Disruption of adaptor protein 2µ (AP-2µ) in cochlear hair cells impairs vesicle reloading of synaptic release sites and hearing

SangYong Jung[1,2,3#], Tanja Maritzen[4,5#], Carolin Wichmann[2,6,#], Zhizi Jing[2,7], Andreas Neef[8,§], Natalia H. Revelo[2,9], Hanan Al-Moyed[2,6], Sandra Meese[2,10], Sonja M. Wojcik[11], Iliana Panou[1,2], Haydar Bulut[4], Peter Schu[12], Ralf Ficner[2,10], Ellen Reisinger[2,13], Silvio O. Rizzoli[2,9,14], Jakob Neef[1,2,3], Nicola Strenzke[2,7], Volker Haucke[4,5,§] and Tobias Moser[1,2,3,14,§]

Inventory:

Appendix Figure S1. Normal cochlear function in *AP-2μ$^{fl/+}$:Cre* and *AP-σ1B$^{-/-}$* mice

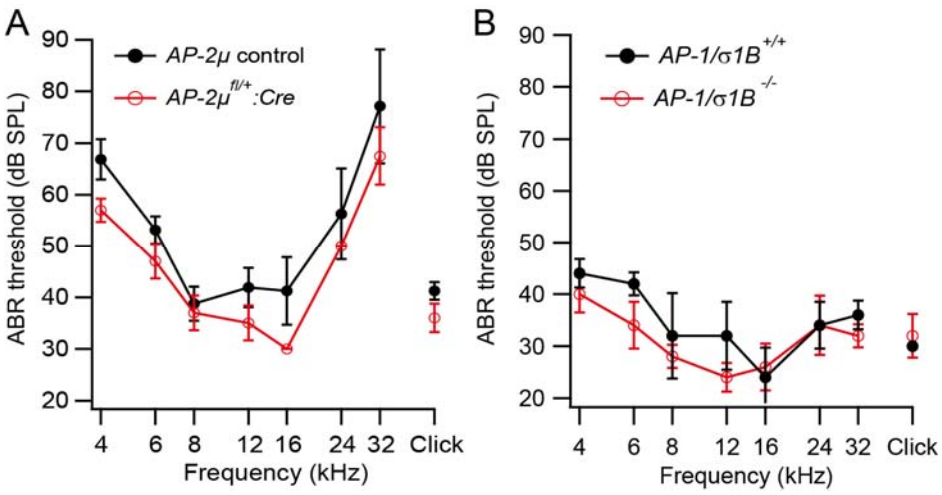

A, Normal ABR thresholds in heterozygous *AP-2μ$^{fl/+}$:Cre* (open red circles, n = 5) compared to *AP-2μ* control (*AP-2μ$^{fl/fl}$* mice, n = 7-9).
B, Normal ABR thresholds of *AP-σ1B$^{-/-}$* mice (red, n = 5) when compared to *AP-σ1B$^{+/+}$* mice (black, n = 5).
In both datasets amplitudes and latencies of all ABR waves in response to 10-100 dB Click stimuli were normal (not shown).

Appendix Figure S2. Normal Ca^{2+} influx and number of afferent synapses of *AP-2μ$^{fl/fl}$:Cre* mice

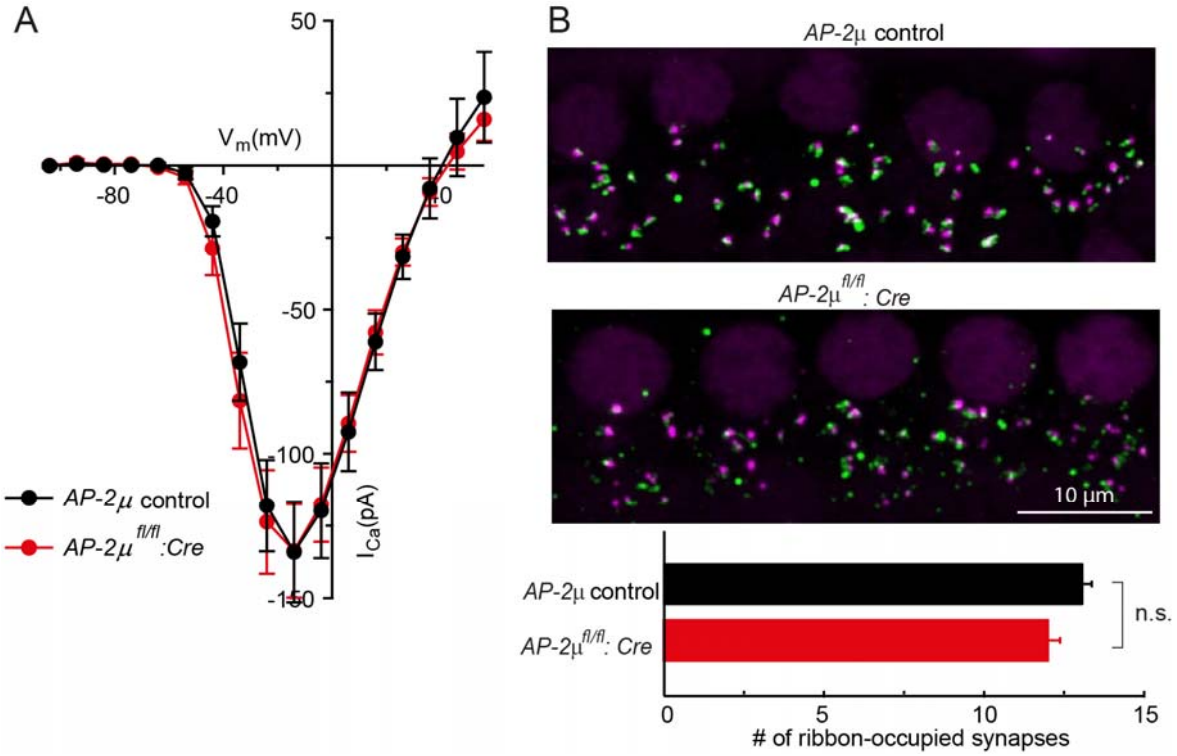

A, Normal voltage-dependence and amplitude of Ca^{2+} influx in IHCs of *AP-2μ$^{fl/fl}$:Cre:GFP* mice (red, n = 15) when compared to IHCs of *AP-2μ* control (black, n = 12)

B, Maximum projection of a stack of confocal sections of organs of Corti of *AP-2μ* control (top) and *AP-2μ$^{fl/fl}$:Cre* (middle) mice following immunolabeling for the ribbon marker CtBP2/RIBEYE (magenta) and the postsynaptic AMPA receptors GluA2/3 (green). The number of afferent synapses (GluA2/3 immunofluorescence puncta in the IHC region) (13.2 ± 0.3 vs. 13.6 ± 0.4) and ribbon-occupied afferent synapses (juxtaposed pre- and postsynaptic immunofluorescence puncta) (bottom, 13.1 ± 0.3 vs 11.9 ± 0.4) was comparable in *AP-2μ$^{fl/fl}$:Cre* (n = 74 IHCs from 4 mice) and *AP-2μ* control (n = 79 IHCs from 4 mice).

Appendix Figure S3. Model fitting of cumulative interspike intervals distribution during adapted firing

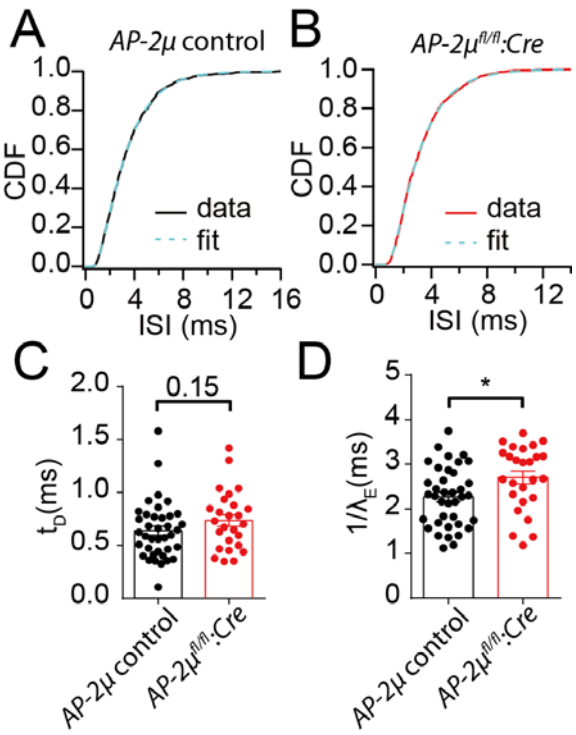

A, B, Representative examples of cumulative ISI distributions for *AP-2μ* control and *AP-2μ$^{fl/fl}$:Cre:GFP* SGNs, taken from the adapted firing period (solid lines). Data were fitted with a three parameter Gamma-Poisson mixture model (dashed lines, (Heil et al., 2007)). The model assumes that excitatory events are driven by a mixture of a Gamma and a Poisson process with a scaling factor λ_E and a fixed shape factor of 2 for the Gamma process. The driven events are further modified by a postsynaptic refractoriness process, which is assumed to be composed of a dead time (t_D, panel C) reflecting the absolute refractoriness and a single exponential recovery of spike probability after t_D (relative refractoriness). The time constant of exponential recovery is fixed to 0.65 ms. λ_E ($1/\lambda_E$, panel D) is a scaling factor of both Gamma and Poisson process.

Appendix Figures S4 & 5. Model-based analysis of forward masking data and interspike-interval statistics of SGN for studying release site function in IHCs

Spiking of a SGN is, in most mammals, exclusively driven by synaptic transmission at a single ribbon synapse between an IHC and the SGN. This makes the spike pattern of the SGN an exquisitely sensitive probe of the vesicle release dynamics of a single active zone. The system can be seen as a presynaptic machinery that produces a stochastic sequence of a excitatory events followed by a spike trigger with refractoriness. The outcome is a sequence of spike times the statistics of which could possibly be very informative about the underlying presynaptic mechanisms. In addition, fitting such models to SGN spike rate data can help determining the dynamics of the properties of the RRP. In the following we briefly summarize the "release site model" that was used in Figure 5 and described in detail before (Frank et al., 2010). Thereafter, we present new modeling that is documented in Figure EV4 and the Appendix Figure S4 and S5 that addresses presynaptic candidate mechanisms explaining the Gamma process contribution to the release statistics.

Release site model of RRP release and replenishment

In brief, the presynaptic vesicle cycling is described from the perspective of docked vesicles. Given the limited surface area of the active zone and the limited number of Ca^{2+} channels in that area, the observation of a Ca^{2+} nanodomain regime motivates the notion of a limited, quasi-fixed number of available release sites or slots, N_{slot} (Wong et al., 2014). Each of these sites can either be occupied by a fusion ready vesicle or not. At each point in time the fusion ready vesicle will fuse with a certain probability described by the fusion rate constant k_{fus}. Its value depends on the sound pressure level. We assume the simplest case of a linear relation for sound pressure levels within the dynamic range of the synapse/fiber. While the sound pressure level rises from threshold to saturation k_{fus} increases from $k_{fus,\ spont}$ to $k_{fus,stim}$. The refilling of empty sites is described by a refill rate constant k_{refill}, which is also stimulus dependent ($k_{refill,\ spont}$ to $k_{refill,stim}$).

The state of the release site is described by:

$$\frac{dN_{slot}^{filled}(t)}{dt} = k_{refill}(t)N_{slot} - N_{slot}^{filled}(t)\left(k_{fus}(t) + k_{refill}(t)\right) \qquad \text{Eq. S1}$$

Although this equation is formulated for vesicle fusion rates, a scaling factor can be used to account for the fraction of fusion events that cannot successfully trigger an action potential (AP) due to the small size of the evoked EPSC. Such a factor f effectively operates as if the number of release sites was scaled down. The scaled equation then gives a rate R of potentially supra-threshold EPSCs as the product of the number of occupied release sites, the fusion rate constant and the scaling factor:

$$R(t) = k_{fus}(t) \cdot f \cdot N_{slot}^{filled}(t) \qquad \text{Eq. S2}$$

The stationary solutions of S1 together with S2 determine steady state occupancy and steady state event rates:

$$N_{slot}^{filled}\Big|_{steady\ state}^{condition} = \frac{k_{refill}^{condition}}{k_{fusion}^{condition} + k_{refill}^{condition}} \cdot N_{slot} \qquad \text{Eq. S3}$$

$$R\Big|_{steady\ state}^{condition} = \frac{k_{fusion}^{condition} \cdot f \cdot k_{refill}^{condition}}{k_{fusion}^{condition} + k_{refill}^{condition}} \cdot N_{slot} \qquad \text{Eq. S4}$$

where “condition” is “stim” or “spont” for silence and saturating sound pressure level, respectively.

In order to connect the postsynaptic event rate of potentially supra-threshold EPSCs to the actual AP rate, refractoriness is considered as a combination of an absolute refractory period t_{abs}, during which the probability of an EPSC to trigger an AP is zero, with a relative refractory period during which this trigger probability returns to 1 with an exponential time course characterized by τ_{rel} (Berry and Meister, 1998). This description of refractoriness can be applied to the ‘driving’ EPSC rate R by means of a delayed differential equation. The equation is motivated by the concept of three possible states of the SGN: ‘absolute refractory’, ‘relative refractory’ or ‘available’. At any point, the probability that the SGN turns from ‘available’ to ‘refractory’ is proportional to the rate R(t). The return back to ‘available’ happens ‘delayed’ by t_{abs} and with a probability that is proportional to $1/\tau_{rel}$.

$$\begin{aligned} \frac{df_{avail}(t)}{dt} &= \frac{f_{relref}(t)}{\tau_{rel}} - f_{avail}(t) \cdot f \cdot R(t) \\ \frac{df_{relref}(t)}{dt} &= f_{avail}(t - t_{abs}) \cdot f \cdot R(t - t_{abs}) - \frac{f_{relref}(t)}{\tau_{rel}} \end{aligned} \qquad \text{Eq. S5}$$

Together with Equation S4 the stationary solution of this description of refractoriness connects the observable steady state rates during silence and stimulation to the rate constants k_{refill} und k_{fusion}:

$$AP\_Rate\Big|_{steady\ state}^{condition} = \frac{k_{fusion}^{condition} \cdot f \cdot k_{refill}^{condition}}{k_{fusion}^{condition} + k_{refill}^{condition}} \cdot N_{slot} \cdot \frac{1}{1 + R\Big|_{steady\ state}^{condition}(t_{abs} + \tau_{rel})} \qquad \text{Eq. S6}$$

To go beyond the description of steady state event rates and to use the model for a parameterized description of the actual time course of experimentally observed peristimulus time histograms acquired during forward masking (PSTH, Figure 5A), it is necessary to define the relation between the applied stimulus and the fusion and refill rate constants. For the experimental data presented here, the stimulus level was increased from silence to 30 dB above fiber threshold within 2.5 ms in a sin² shape. On average the fibers had a threshold of about 30 dB and a dynamic range of about 20 dB. That means that the section of the stimulus that effectively increases the AP rate had a

duration of 0.6 ms. It was assumed that k_{fusion} and k_{refill} follow the stimulus increase simultaneously. The offset of the PSTH was best described when the fusion rate constant dropped back to its spontaneous level with a small delay, equivalent to a 1 ms time constant. k_{refill} was treated the same way. The ordinary differential and delayed differential equations above were combined in a fit function. PSTHs were averaged to obtain 1 PSTH per genotype for each masker probe interval. All PSTHs for one genotype were fit in parallel with 1 parameter set.

Modeling functional states of the release site for studying the presynaptic mechanisms that govern spike time statistics

The statistics of the time intervals between certain events, e.g. release events (inter-event interval, IEI) or spikes (interspike intervals, ISI) follows an exponential distribution if, and only if, the event generator has no memory and is instantly reset. In this case, the timing of the next event is independent of any previous event time. So even after an unusually long period without an event, the probability of an event occurring in the next milliseconds never changes. Radioactive decay is a prime example of a memory less system that follows a Poisson process and produces exponentially distributed IEI. There is one obvious reason why the ISI of spiral ganglion neurons should not behave like a memory less generating process: the postsynaptic spike trigger displays refractoriness as sodium channels have to recover from inactivation before the next spike can be fired. This is often well described by an absolute refractory period, during which a synaptic excitatory event can never lead to a spike, and a following relative refractory period, during which the firing ability returns to baseline with an exponential time course. But even when we account for the properties of the refractory process, the analysis of the ISI distribution suggests that the underlying process that generates the excitation events, i.e. vesicle release events, deviates from the memory less Poisson process.

Heil and colleagues (Heil et al., 2007) demonstrated that better description of the data is obtained, if the excitatory process is described as a mixture of a Poisson process and a Gamma process with a shape factor of 2. They noted that this is equivalent to pruning individual events from Poisson train, whereby never two or more successive events are removed. On the one hand it should be no surprise that the process of vesicle release is not without a memory: after the release of a vesicle, a number of steps are required before a vesicle can be released again from the same site. These steps, e.g. site clearance or docking and priming of another vesicle, will consume some time and hence represent some memory of the past release event. On the other hand, vesicle release from different release sites or ‘slots’ might be independent from each other, which would warrant some degree of independence of vesicle release events, at least for a sufficiently large number of release sites. Indeed, models based on a Poisson driven vesicle release can capture the core aspects of the spike dynamics of SGNs (Buran et al., 2010).

We performed simulations of ISI of SGN based on conceptually different models of the functional states of the release site, which can be considered a cycle of states (Andor-Ardo et al., 2010). Each of N_{slot} identical slots can be in one of N different states, such

as ‘1 - full’ and ‘2 -released’ in the example of a 2 state model or ‘1 - cleared’, ‘2 - docked’, ‘3 - primed’ and ‘4 - released’ in a four state model. The transitions between the states can be either exponential (Figure EV4A) or they could be characterized by a fixed lag time (Figure EV4B). The latter would be expected for transitions that are driven by diffusion or represent a large number of substeps. When a transition into the ‘released’ state occurs, an excitatory event is registered. Events from different slots are indistinguishable. As long as only 1 active site generates release events, the details of vesicle release and refill kinetics are clearly reflected in the statistics of the IEIs (Figure EV4C, D). As the number of release sites increases, the IEI distributions become more uniform, mostly resembling a mixture of Gamma and Poisson processes (Figure EV4E).

Given the time points of all release events from all slots, individual events are pruned representing the triggering of spikes by a mechanism with the refractory properties described for SGNs (Heil et al., 2007; Miller et al., 2001, 2006). The cumulative ISI distribution (CDF_{ISI}) is then fit by a mixture of Poisson- and Gamma (2) - driven events followed by refractory transmission. The respective fit function is

$$CDF_{ISI}(t) = 1 - \frac{1}{\lambda_E - 1/\tau_{rel}} \cdot \left[\left(\lambda_E \cdot \exp(-(t - t_{abs}/\tau_{rel}) - 1/\tau_{rel} \cdot \exp(-(t - t_{abs}) \cdot \lambda_E \right) \cdot \left(1 - b + \frac{b \cdot \lambda_E}{\lambda_E - 1/\tau_{rel}} \right) \right.$$

$$\left. - b \cdot \frac{\lambda_E}{\tau_{rel}} \cdot \exp\left(-(t - t_{abs}) \cdot \lambda_E\right) \cdot \left(t - t_{abs} + \frac{1}{\lambda_E} \right) \right]$$

Eq. S7 (Heil et al., 2007; Li and Young, 1993)

for $t > t_{abs}$ and 0 for $t <= t_{abs}$.
The parameters are:

t_{abs} ... absolute refratory period

τ_{rel} ... relative refratory period

λ_E ... rate of the excitatory processes (Gamma and Poisson)

b ... fraction with Gamma(2) character

When we simulated interspike intervals driven by a mixture of a Poisson process and a Gamma process, a fit with this equation could retrieve the original parameters used for the simulation when care was taken to fix t_{abs} from the shortest ISIs (Li and Young 1993). We did observe some cross-talk between the parameters τ_{rel} and *b* as both influence the shape of the cumulative distribution for small ISIs. However, as *b* also exerts some influence on the long ISI tail, typically the fit results were within +/- 20% of the original values. The following Figures explain the concepts behind the simulations.

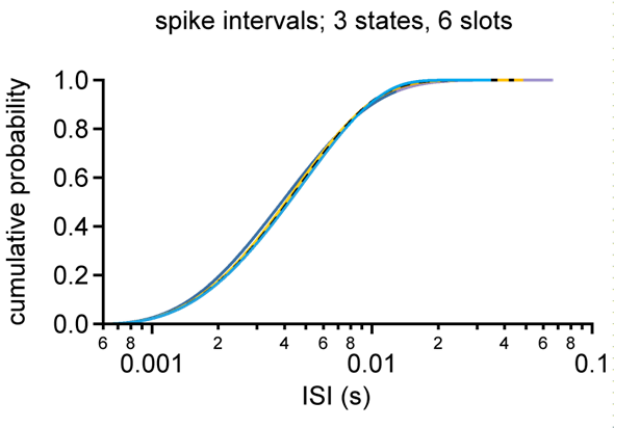

Release site characteristics	Gamma fraction	λ_E (s^{-1})
$k_1, k_2 >> k_3$	0.0	265
$k_1 >> k_2, k_3$	0.39	373
$k_1 = k_2 = k_3$	0.45	385
t_1 = const.; $k_2 = k_3$	0.48	386

Appendix Figure S4: Fits to the cumulative density function of ISI

Over a wide range of rates, waiting times and slot numbers the resulting CDFs can be well described with equation S1. The fit parameter 'Gamma fraction' is sensitive to changes of the release site model.

Conclusions

Analysis of the interspike-interval (ISI) distributions from *AP-2μ* control and *AP-2μ$^{fl/fl}$:Cre:GFP* mutants revealed a difference in the prevalence of the Gamma and the Poisson characteristics. In *AP-2μ$^{fl/fl}$:Cre:GFP* mutants the ISI distribution had a stronger Gamma-like component. As explained above, only a few parameters of the systems have an influence on the expression of this Gamma characteristics.
The objective of the simulations was to understand which properties of the vesicle release and spike trigger system could lead to an increase in the Gamma-weight. Figure EV4E indicates that a decrease in the number of release sites increases the Gamma-like component in the IEI distribution and further simulation confirmed that this is indeed the case even when the release events go through the refractory spike detector. For the example of release sites with 3 identical states, the Gamma fractions for release through 3, 6, 9, 12 and 15 slots are 0.66, 0.45, 0.36, 0.29 and 0.22 as estimated by fits with equation S1. A number of different analyses, such as vesicle counts in electron microscopy, capacitance transients in patch-clamp and the analysis of post-stimulus time histograms to tone-bursts, all suggest that the AP-2 deficient mice have only a slightly reduced number of release sites. Therefore, the majority of the observed increase in the Gamma fraction in the ISI analysis is due to an altered statistics at the individual release sites. Any change that *increases the number of rate determining steps* in the release/refilling cycle has such an effect on the Gamma fraction. An example for the case of 9 release sites with 4 states can illustrate this (Appendix Table S1).

slot characteristics	N	Gamma fraction *b*	λ_E (s^{-1})	Spike rate (Hz)
t_1 = 0.9 ms; **k_2 = 24.4 s^{-1}**; $k_3 = k_4$=3000 s^{-1}	11	0.12	258.5	200 Hz
t_1 = 0.9 ms; **k_2 = 24.4 s^{-1}**; k_3 = 3000 s^{-1}; **k_4 = 56 s^{-1}**	9	0.38	132	115 Hz
t_1 = 26.6 ms; **k_2 = 24.4 s^{-1}**; $k_3 = k_4$ = 3000 s^{-1}	9	0.38	132	115 Hz
t_1 = 0.9 ms; **k_2 = 15 s^{-1}**; $k_3 = k_4$ = 3000 s^{-1}	9	0.093	132	115 Hz

Appendix Table S1. Simulated ISI distributions, driven by activity of 9 release sites with 4 states each, were fitted with equation S1. Those transitions that contribute to limiting the overall rate of the release/refill cycle are shown in bold. Alterations to the reference model in the first row are shown in red.

The example clearly demonstrates that not just any parameter change that reduces the release rate also increases the gamma fraction. Instead, an increase in *b* indicates that the number of those transitions that limit the overall rate has increased. The IEIs capture the kinetics of the *entire* release/refill cycle. From those stationary state statistics it is not possible to draw conclusions about which transition of the cycle has been altered by AP-2 deficiency. But the results suggest that at least one step that had not been the kinetic bottleneck in the control animals does slow the release/refill cycle in the AP-2 deficient mice. It is tempting to speculate that the increased Gamma fraction seen in the ISI distributions of SGNs of *AP-2$\mu^{fl/fl}$:Cre:GFP* mice results from disruption of AP-2/otoferlin-mediated facilitation of active zone clearance, be it via an additional rate-limiting step or as a fixed dead time or refractoriness of the presynaptic release site.

Appendix Figure S5: Modeling diffusional clearance of membrane proteins out of the fusion zone

Before fusion, part of the proteins involved reside in the vesicle membrane, others in the AZ. This spatial distribution is instrumental in coupling the Ca^{2+}-binding to fusion. After fusion the entire protein complex is localized to the plasma-membrane of the AZ. The once vesicular and the once AZ proteins are still bound to each other; leaving no valences for newly arriving vesicles to engage with AZ partners. In order to make the release site ready for the next vesicle, the proteins from recently fused vesicles have to disengage from their AZ partner proteins or new copies of these AZ proteins have to diffuse in and become available at the release site. The details of the dynamic equilibrium between (un-)binding and diffusion are not clear. Nevertheless, it is interesting to consider the time-course of protein diffusion in the membrane, which for exocytosed vesicular proteins could rate-limit the "freeing up" of AZ proteins. The governing parameters is the diffusion coefficient D. A highly quantitative method to determine D is *dual-focus* fluorescence correlation spectroscopy. For small proteins D is on the order of 9 µm²/s, provided a completely undisturbed diffusion at very small protein concentrations (Weiß et al., 2013). Already the effect of crowding can slow effective diffusion by factors of 2 to 5 (Guigas & Weiss, 2014). In addition, protein movement under physiological conditions often displays more than one spatial or temporal scale, reflecting trapping in different lipid phases or transient binding between the diffusing molecule and immobile binding partners (Mueller et al., 2011). This results in anomalous diffusion for which the effective D depends on the timescale of observation and can be orders of magnitude smaller than the D for free diffusion. For the case of transient binding to immobile partners (such as proteins of the AZ) the slowing can readily be estimated: for association and dissociation rates k_{on}, k_{off} the fraction of time spent in free diffusion is $f_{free} = k_{off}/(k_{on} + k_{off})$ and the effective D is $D = D_{free} \cdot f_{free}$. As we have little information about the binding of fusion machinery proteins to immobile AZ proteins after fusion, we will restrict the discussion of diffusion times to the fast, free diffusion. However, even this way of clearing the release zone could be accelerated, if the newly fused protein was captured or converted into an inactive form at a boundary. This would prevent the protein from re-entering the release zone, where it could interfere with the site replenishment, i.e. the binding of protein atop newly arriving vesicles.

In order to quantitatively assess fusion zone clearance by diffusion, a few parameters have to be fixed. Besides the diffusion coefficient D_{free}, 9 mm²/s (Weiß et al., 2013), the area that has to be cleared needs to be defined. At the inner hair cell ribbon synapse, vesicles are docked at lines at both sides along the elongated ribbon tethering area (Figure 6 in main manuscript). Fusion will occur inside these two stripes which are a few hundred nanometers long and one vesicle diameter, i.e. 50 nm, wide. A protein exits a

stripe by diffusion perpendicular to the stripe, away from the ribbon. Diffusion in parallel to the ribbon can be neglected, as this distance is much longer than the width to the fusion zone. Diffusion across the AZ center (presynaptic density) is also not very likely as this region likely constitutes a diffusion barrier. With these considerations, we can look at one-dimensional diffusion of a substance, deposited at time t = 0 at position x = 0. A reflective boundary at x=0 represents the impermeable tether zone. One possible variation is the presence of an absorptive border at x = 50 nm, where protein that has diffused to this boundary is captured or possibly inactivated in order to prevent re-entering into the 50 nm stripe.

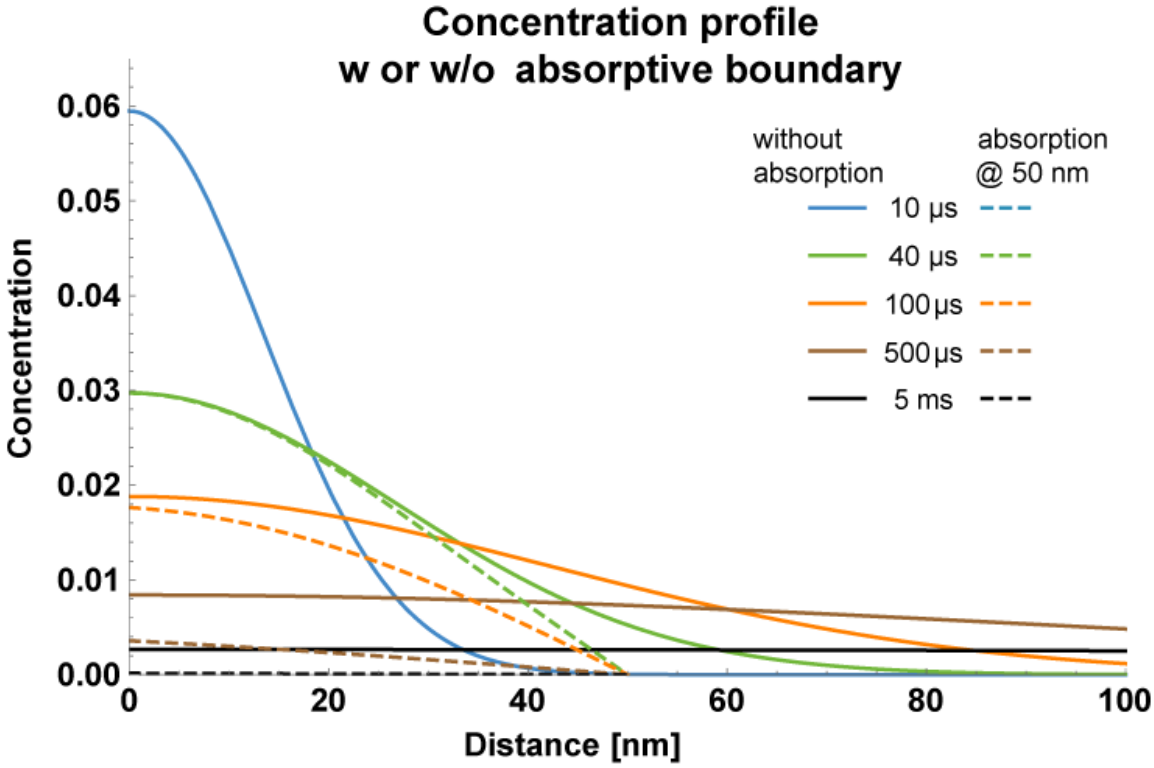

Appendix Figure S5: Diffusion away from the fusion site
For a molecule with a diffusion coefficient of 9 µm²/s, the putative border of the fusion zone, 50 nm from the fusion site, is not reached before 20 ms after fusion. After this time point, the presence of an absorptive boundary would speed up the clearance of the 50 nm zone. This can be seen as the dotted lines are below the continuous lines of the same color.

References

Andor-Ardo, D., Hudspeth, A.J., Magnasco, M.O., and Piro, O. (2010). Modeling the resonant release of synaptic transmitter by hair cells as an example of biological oscillators with cooperative steps. Proc. Natl. Acad. Sci. *107*, 2019–2024.

Berry, M.J., 2nd, and Meister, M. (1998). Refractoriness and neural precision. J. Neurosci. Off. J. Soc. Neurosci. *18*, 2200–2211.

Buran, B.N., Strenzke, N., Neef, A., Gundelfinger, E.D., Moser, T., and Liberman, M.C. (2010). Onset coding is degraded in auditory nerve fibers from mutant mice lacking synaptic ribbons. J. Neurosci. Off. J. Soc. Neurosci. *30*, 7587–7597.

Frank, T., Rutherford, M.A., Strenzke, N., Neef, A., Pangršič, T., Khimich, D., Fejtova, A., Gundelfinger, E.D., Liberman, M.C., Harke, B., et al. (2010). Bassoon and the synaptic ribbon organize Ca^2+ channels and vesicles to add release sites and promote refilling. Neuron *68*, 724–738.

Heil, P., Neubauer, H., Irvine, D.R.., and Brown, M. (2007). Spontaneous activity of auditory-nerve fibers: insights into stochastic processes at ribbon synapses. J. Neurosci. *27*, 8457.

Li, J., and Young, E.D. (1993). Discharge-rate dependence of refractory behavior of cat auditory-nerve fibers. Hear. Res. *69*, 151–162.

Miller, C.A., Abbas, P.J., and Robinson, B.K. (2001). Response properties of the refractory auditory nerve fiber. JARO-J. Assoc. Res. Otolaryngol. *2*, 216–232.

Miller, C.A., Abbas, P.J., Robinson, B.K., Nourski, K.V., Zhang, F., and Jeng, F.-C. (2006). Electrical Excitation of the Acoustically Sensitive Auditory Nerve: Single-Fiber Responses to Electric Pulse Trains. J. Assoc. Res. Otolaryngol. *7*, 195–210.

Weiß, K., Neef, A., Van, Q., Kramer, S., Gregor, I., and Enderlein, J. (2013). Quantifying the diffusion of membrane proteins and peptides in black lipid membranes with 2-focus fluorescence correlation spectroscopy. Biophys. J. *105*, 455–462.

Wong, A.B., Rutherford, M.A., Gabrielaitis, M., Pangrsic, T., Göttfert, F., Frank, T., Michanski, S., Hell, S., Wolf, F., Wichmann, C., et al. (2014). Developmental refinement of hair cell synapses tightens the coupling of Ca2+ influx to exocytosis. EMBO J. *33*, 247–264.